Proceedings of ASME Turbo Expo 2011
GT2011
June 6-10, 2011, Vancouver, British Columbia, Canada

GT2011-46009

NUMERICAL INVESTIGATION OF A NOVEL AXIAL IMPELLER AS PART OF A COUNTER-ROTATING AXIAL COMPRESSOR TO COMPRESS WATER VAPOR AS REFRIGERANT

Qubo Li
Mechanical Engineering Department
Michigan State University
East Lansing, MI, liqubo@egr.msu.edu

Zachariah Alan Sprinkle
Mechanical Engineering Department
Michigan State University
East Lansing, MI, sprinkl6@msu.edu

Janues Piechna
Institute of Aeronautics and Applied Mechanics
Warsaw University of Technology
Warsaw, Poland

Norbert Mueller
Mechanical Engineering Department
Michigan State University
East Lansing, MI, United States

ABSTRACT

A systematic investigation to understand the use of a novel axial impeller, as a part of counter rotating axial compressor used to compress water vapor as refrigerant is undertaken. Blade angle and construction is investigated to understand this novel impeller's geometry. A commercial CFD package, which solves the Reynolds-averaged Navier-Stokes equations, is used to compute the complex flow field of the impeller. Two nondimensionalized "hub-diameter/shroud-diameter" ratios (H_d/S_d) with different speed ratios are numerically simulated for comparison. The numerical simulation focused on the water vapor flow from compressor impeller inlet to outlet and the overall performance level and range are predicted. The numerical investigation reveals that at hub/shroud H_d/S_d tip ratio of 0.54, the maximum pressure ratio reached 1.24 with an isentropic efficiency near 75% at its design point. Detailed investigation into flow structure shows that a serious secondary flow existed between blade span ranges of 30% to 50%. An enlargement of H_d/S_d ratio to 0.75 shows that the pressure ratio had been improved significantly. By comparing different speed ratios and hub/shroud tip ratios, the study shows the potential to successfully utilize this novel axial impeller to compress water vapor as refrigerant.

INTRODUCTION

An application of the investigated preliminary compressor design is in the mechanical compression refrigeration units that utilize water (R718) as refrigerant. The use of water as a refrigerant in vapor compression systems offers several potentially significant advantages because it fulfills most of the fundamental requirements of a refrigerant [1]. The first main advantage of using water as refrigerant is that it is a green refrigerant: it is environment friendly, nontoxic and non-flammable. Besides these, as a green refrigerant it has zero ozone depletion potential (ODP) and zero global warming potential. Therefore there are no direct risks associated with using water as a refrigerant in the future. The second main advantage of using water as a refrigerant is that it is a naturally occurring substance: it can be obtained for free and is readily available. Dirtied water is easily cleansed and clean water is disposable. The more important characteristics of water include the fact that it has a potential to save energy; about 20-30% over conventional refrigerants [2] when used in proper mechanical compression refrigeration units.

Compressing water vapor to use as a refrigerant imposes specific challenges for the compressor designer. For example, the pressure ratio across an impeller needs to be as high as 6, which is about two or three times that of conventional refrigerants (like R134a). In addition, the compressing of water vapor has to be conducted under near-vacuum conditions, which varies between 900Pa and 1,800 Pa. Such a low pressure produces the need for a very large volume flow rate for within the compressor, due to the decrease in gas density [3]. Many common impellers struggle to maintain such a high pressure ratio and volume flow rate, causing industry to shy away from the use of R718.

To overcome these challenges, a novel axial composite impeller has been developed at Michigan State University [4-

8]. Since this kind of novel composite impeller can be manufactured through a filament-winding, similar technology, impeller manufacturing costs have been reduced greatly. In addition, the axial impeller has several special characteristics differing from traditional impellers: their blades cross over each other to form special patterns, and they have a constant thickness-to-chord ratio from leading edge to trailing edge. Besides these, one-dimensional blade angle optimization design is dependent on geometry at the shroud, due to the fact that the blades don't necessarily meet the wheel's center. Therefore, blade angle distribution is thus determined by the wheel's pattern and shroud geometry. The impeller investigated has been equipped with a flow shroud, from which the denominator of the "H_d/S_d" ratio comes. This flow shroud inhibits the flow of the working fluid through the center portion of the impeller.

Demiss [2] proposed the concept of utilizing several counter rotating impeller stages to compress water vapor under the vacuum, as is shown in Fig. 1. The use of counter rotating impellers is one of the promising approaches for substantial improvement in aerodynamic performance of an axial-flow compressor. Because of the counter rotating technique, kinematic energy in the tangential direction can be converted into static pressure. This method of a counter rotating system also removes the need for stationary guide vanes in a compressor, as they would be replaced by a counter rotating compression stage. Accordingly, the size of the compressor system can potentially be decreased. Because of this advantage, the counter rotating technique has been studied in aviation primarily for the compression of air.

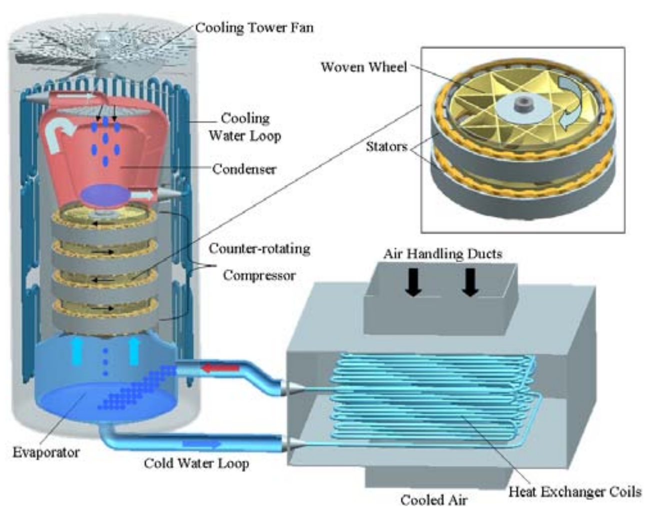

Figure 1 Turbo chiller compressing water vapor as refrigerant [2]

Chen [9] numerically and experimentally investigated the speed ratio's effect to rotor's optimal performance in terms of both pressure ratio and isentropic efficiency. In Chen's work for the designed impeller, it is found that by adjusting each wheel's rotating speed, a proper incidence angle is found to be the most significant factor influencing the optimization of performance. Some other studies, such as the one conducted by Young [10], focused on systems of counter rotating impellers moving at equal speeds. Here design performances are not explored in the work. To apply this technology and novel axial impeller into a water vapor compressor, this paper will first investigate its possibilities and challenges from aerodynamic views.

The blades in the novel axial impeller do not meet in the wheel's center. Therefore, blade shape and orientation at the shroud, as well as the winding pattern, determine the entire wheel's blade-angle distribution. With this complexity, one- and two-dimensional angle optimization methods cannot work. For this special impeller, numerical methods become the main approach to optimizing blade angle. Numerical approaches through CFD (Computational Fluid Dynamics) have been widely recognized as a powerful method for predicting the performance and understanding the fluid flow characteristics for axial impellers [11-13].

The purpose of the present study is to use a CFD approach to investigate one single, counter- rotating, axial impeller compression stage, being used to compress water vapor as refrigerant. In the following studies, once a specific impeller design is selected, then further numerical simulations will be performed. These will involve multiple stages with a water inter-cooling (flashing) strategy. In such a way, optimization will occur for one single, counter- rotating stage; multiple stages; then an entire compressor system, before building the compressor and testing its performance. For this reason, a description of impeller geometry and of blade angle will be given at first. A 3D CFD approach will be then used to optimize blade angle for specific mass flow rate and Mach number requirements. Based on CFD optimized blade angles, the speed ratio's effect will then be discussed and the flow characteristics for H_d/S_d ratios will be investigated to better design this impeller as part of water vapor refrigerant compressor. Finally, a conclusion is drawn and design and optimization-related suggestions are given.

Investigated impeller geometries

A specific impeller pattern, "8C", is designed and manufactured using a filament winding similar technique. This impeller geometry is used throughout the report and can be seen as a circumscribed eight-point star, in figure 1 to the left. This design is selected from various patterns based on preliminary aerodynamic performance comparisons conducted [5, 7]. This pattern is discovered to have its own special characteristics, which make them different from conventional rotors: constant thickness-to-chord ratio from leading edge to trailing edge, and the camber line at the shroud is a circular arc. This arc can be one-dimensionally optimized, affecting blade angle and angles of the blade between shroud and inner hub. These are also determined by the filament winding pattern and can be analytically calculated. Constant thickness-to-chord ratio has been known to create serious boundary layer separation problems, considering subsonic fluid mechanics.

However, these novel impeller patterns have small triangular channels, which guide and benefit the fluid flow [7]. Fig. 2 shows the overall view of the investigated composite 8c impeller with two different H_d/S_d ratios: 0.54 and 0.75. Here you can note that the wheels are identical with the exception of the hub diameter.

The impeller has 16 non-radial blades. Since they are non-radial and the blades do not meet at the wheel's center but at the shroud, conventional design optimization approaches (such as one-dimensional and two-dimensional optimization methods) are not equipped to deal with this specific pattern. Therefore usual optimization techniques will not work. Because of this, a three-dimensional CFD method is utilized to optimize the blade angle for the best performance, in terms of pressure ratio and isentropic efficiency for both impellers. Designed rotating speed is decidedly 7,000RPM under vacuum conditions.

From specific manufacturing principles, the impeller is woven by crossing slots on a mandrel, where circular arcs are evenly distributed. Therefore blade angle distribution is determined by the arcs connecting the slots on the winding mandrel. Interested readers can refer to detailed patented manufacturing processes and pattern description in related publications [4-7].

Given the axial blade angle at leading and tailing edge, β_{inlet} and $\beta_{outlet,}$ on the shroud and the axial length of the arc $L_{ax} = y_{outlet} - y_{inlet}$ determines the camber line at any axial height in Fig.3. For four points marked in Fig.3, their coordinates can be expressed as

$$\begin{aligned} x_1 &= R \times \cos\left(\frac{r \times \cos\beta_{inlet}}{R}\right) \\ y_1 &= R \times \sin\left(\frac{r \times \cos\beta_{inlet}}{R}\right) \\ z_1 &= r \times \sin\beta_{inlet} \end{aligned} \tag{1}$$

$$\begin{aligned} x_2 &= R \times \cos\left(\frac{r \times \cos\beta_{inlet} + n \times l}{R}\right) \\ y_2 &= R \times \sin\left(\frac{r \times \cos\beta_{inlet} + n \times l}{R}\right) \\ z_2 &= r \times \sin\beta_{inlet} \end{aligned} \tag{2}$$

$$\begin{aligned} x_3 &= R \\ y_3 &= 0 \\ z_3 &= 0 \end{aligned} \tag{3}$$

$$\begin{aligned} x_4 &= R \times \cos\left(\frac{n \times l}{R}\right) \\ y_4 &= R \times \sin\left(\frac{n \times l}{R}\right) \\ z_4 &= 0 \end{aligned} \tag{4}$$

Therefore,points 1 and 2 determine any point located at the leading edge such that

$$f_{leading}(x,y,z)=f(\text{point 1, point 2})$$

Also point 3 and 4 determine any point located at the trailing edge such that

$$f_{trailing}(x,y,z)=f(\text{point3, point4})$$

The angle of the blades connecting the leading edge and trailing edge can thus be expressed as

$$\theta = \arccos\left(\frac{z_{leading}(t) - z_{trailing}(t)}{\sqrt{(x_{leading}(t) - x_{trailing}(t))^2 + (y_{leading}(t) - y_{trailing}(t))^2 + (z_{leading}(t) - z_{trailing}(t))^2}}\right) \tag{5}$$

where t changes from 0 to 1, meaning that the point on the leading edge moves from point 1 to point 2, or on the trailing edge where the point moves from 3 to 4. The parameter 'n' is determined weaving process for different impeller blade patterns. In this study for the 8C pattern, 'n' here equals three, whereas other patterns have a different 'n'. Only specific 'n's will work for forming an impeller and this is not discussed here. You may refer to previous publications for further discussion [4-7].

Based on the equations above, the blade angle, from inner hub to shroud, is plotted in Fig. 4. For the optimized blade angle this relationship is a curve, not a straight line like the one in conventional axial impellers where blade angle is optimized for a certain incidence angle. In this paper, incidence angle is defined as the angle difference between absolute fluid flow and axial direction. Blade 1 and blade 2 are symmetric to each other about blade center (not at wheel's center), while blade 3, which meets blade 1 on the shroud has the same blade angle as blade 1. Therefore, it is discussed that only on some specific radius the expected incidence angle can be realized. This is another difference between conventional impellers and the one investigated [7]. For this special impeller, a flow shroud has been integrated with the wheel. At the end wall, the region flow is characterized as very complex flow structures; therefore in this work, no attempt is made to evaluate the impeller's clearance effect within the stage. However, this may potentially have significant contribution to the stage's performance, and it would be an important issue for future investigation[6].

Figure 2 8C impellers with hub/shroud ratio of 0.54 (left) and 0.75 (right)

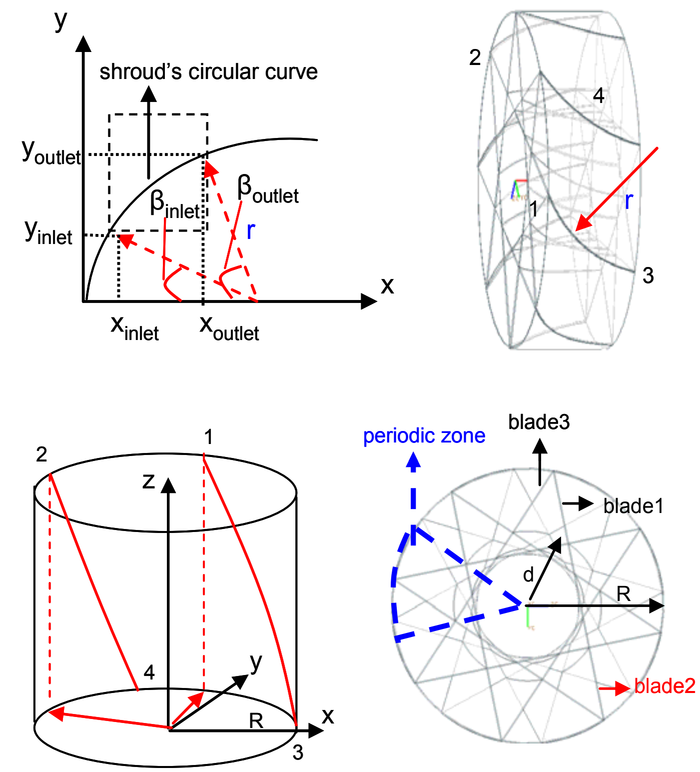

Figure 3 Axial-line blading without hub

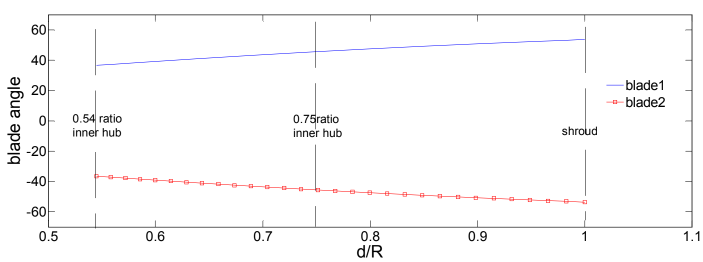

Figure 4 Blade angle along radial direction

Numerical Model Setup

For all the investigated rotor geometries, the flow field around the blade is computed using the commercial CFD code FLUENT [14], where the 3D Reynolds-Averaged form of the Navier-Stokes equations are solved using a finite-element-based, finite-volume method. The 3D mesh of the flow channel was meshed automatically in GAMBIT in Tetrahedral/Hybrid elements. A grid dependency study is also carried out by locally refining the grids in the channel. When the total number of grids increases up to 50%, less than 1% difference has been found in the results. Such a small difference in terms of the pressure ratio and temperature can be considered negligible. Steady-state solutions are computed using the κ-ε turbulence model [15] along with standard, wall functions. In order to increase the accuracy of results, the second-order (highly accurate) upwind differencing method, for the convection terms of each governing equation, is used to minimize the cross-stream numerical diffusion. The second-order accuracy is also maintained for the viscous terms. The pressure velocity coupling is handled by the SIMPLE algorithm. The convergence criterion requires that the scaled residual decreases to 10^{-3} for all of the governing equations, with the exception of the energy equation where residual criteria for convergence decreases to 10^{-6}. To achieve convergence criterion, a relaxation factor for pressure is 0.5 to avoid the correction divergence.

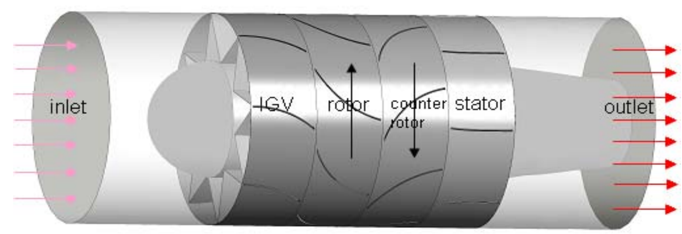

Figure 5 Three-dimensional setup of counter rotating wheels

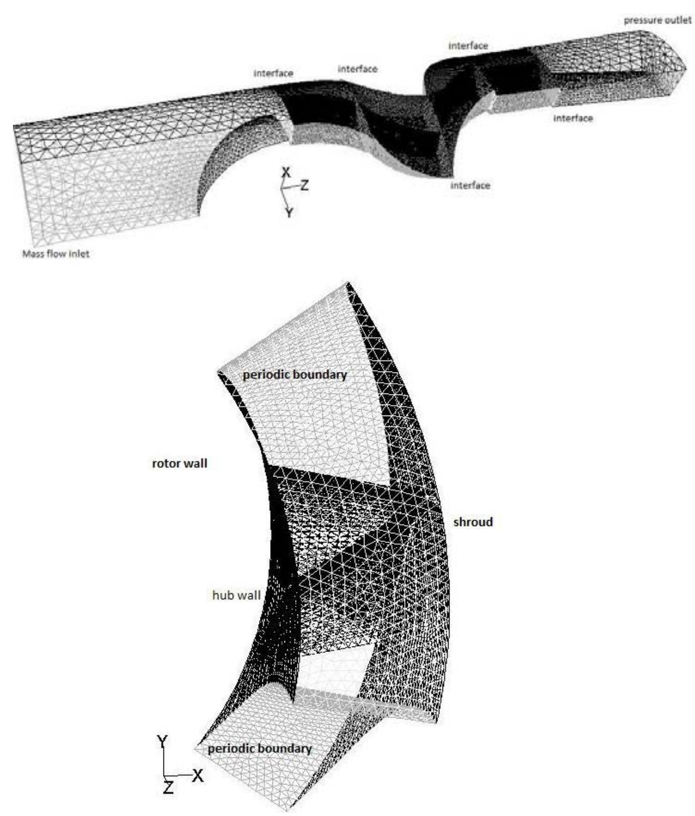

Figure 6 Computational mesh of one flow channel

In order to improve calculation speed and efficiency, only one flow channel with periodic zones, illustrated in Fig.3, is simulated in this work. Also, this flow channel is one eighth of the whole flow zone, shown in Fig.5 with the mesh illustration in Fig.6, and it is symmetric to other identical parts along with flow direction. Surfaces normal to circumferential direction are defined by rotational periodic boundary conditions. For this compressible flow, the inlet mass flow rate is set at the inlet surface with an operational total temperature of 300K. At the inlet, turbulence level is equal 10% with a turbulent length scale of 0.005m are used. At outlet, the desired static pressure is defined. Domains where fluid flows through the channel are set as a reference frame model; rotor and counter rotor wheels are rotating at set RPMs, which are always in opposite directions. Interface boundary conditions are set for each coupled surface between each impeller's upstream and downstream sections. Near solid walls, the standard wall function is used. During all calculations the range of turbulence y^+ values are between 31 and 290, which is acceptable for the standard wall function [14]. Blades of each impeller channel are treated as walls and shrouds are adiabatic.

In order to obtain a steady-state performance map for different cases, several assumptions are made. Oscillations of the flow parameters with an iteration indicate that the compressor is at an operating point close to stall at the left side of characteristic maps. Even though the surge point cannot be accurately predicted using steady-state CFD, the simulation is consistent with terms describing the onset of stall. The right ends of the characteristic maps are defined as the maximum relative Mach number reaches 1. Based on the same criteria, both the performance in terms of the pressure ratio and efficiency and the width of the stable operating range of different cases can be compared consistently.

Results and Discussion

The comparison of performance maps for two different H_d/S_d ratios is given in Fig.7 through Fig.13. The calculation uses the dimensionless quantities of pressure ratio Π (equation [5]), isentropic efficiency η_C (equation (6)) and mass flow rate χ (equation [7]). Since specific heat ratio for water vapor which is computed as ideal gas, varies less than 1% during compression, it is assumed to be constant in Eq. 6. Similar approaches in air radial compressor research has been used by others [16]. Stage total pressure ratio (Π_C) and isentropic efficiency (η_C) of the compressor are calculated based on the total pressures (P_{total}) and total temperatures (T_{total}) at both inlet and outlet of the compressors.

$$\Pi_C = \frac{p_{total-outlet}}{p_{total-inlet}} \tag{5}$$

$$\eta_C = \frac{\left(\Pi_C\right)^{0.254} - 1}{\dfrac{T_{total-outlet}}{T_{total-inlet}} - 1} \tag{6}$$

$$\chi = \frac{\dot{m}}{\dot{m}_{ref}} \frac{p_{t1-ref}}{p_{t1}} \sqrt{\frac{T_{t1}}{T_{t1-ref}}} \tag{7}$$

Thus, it is total-to-total pressure ratio and efficiency. For temperature and pressure, mass-averaged values are used at the outlet. The overall performance of the compressor with different speed ratio (r = speed of rotor/speed of counter rotor) is shown in Fig.7 for 0.54 hub/shroud tip ratio. When the speed ratio is the largest (at r>1 meaning the counter rotating wheel rotates the fastest) the whole stage produces the highest pressure ratio. On the other hand peak efficiency and stable operating range are the lowest among higher speed ratios.

The same phenomenon has also been observed when r<1. With the H_d/S_d ratio of 0.75, the performance curves are likewise illustrated in Fig. 13 and 14 where a significant pressure ratio increased compared with the 0.54 hub/shroud tip ratio. In order to understand the results shown, in the following sections two H_d/S_d ratio cases are investigated separately, and the flow characteristics are analyzed. Based on the analysis of the CFD results, the advantages of utilizing this novel axial counter rotating impellers setting and the optimization of stage configurations will be described.

Case 1 0.54 hub-diameter/shroud-diameter ratio

In Fig.6, to the right, we investigate the case where r<1 such that the counter rotating stage runs faster than the primary rotating stage. As is shown in Fig.6, there is a direct relationship between counter rotating speed and pressure ratio. This can be attributed to higher tangential velocity, which adds the largest kinetic energy thus improving the pressure ratio after a final stationary guide vane. When the speed ratio is less than 1, efficiencies at the peak point decreases when counter rotating speed increases.

In Fig.7, where we investigate the case where r>1, we can see that pressure ratio rises when counter rotating wheel's speed increases, while peak efficiency doesn't vary significantly when speed ratio changes. In addition, the stable working range narrows when the counter rotating wheel speeds up. This can be attributed to the rapid increase of Mach number in this section of the compressor, where choke conditions may occur in the channel. Thus a shorter stable working range is available in comparison to other scenarios. This is one of challenges for counter rotating technology: when a higher pressure ratio is desired, a wider stable working range is required.

Fig.9 compares circumferentially-averaged relative inlet flow angles at different rotating speed's stall points, when counter rotating speed increases from 7000RPM to 10,000RPM. In the figure, blade angle's distribution has been converted from Fig.4, where hub position at H_d/S_d ratio of 0.54 is marked as starting at the x axis in Fig.9. At the designed point with two wheels rotating at 7,000RPM, for this special blade the incidence angle is matched with flow only on blade position; in this figure an *optimum* incidence angle exists around 30% blade span (where blade angle and flow angle meet). This flow angle keeps increasing until 45% span where it drops down until 50% span. Incidence angle's fluctuation can be expected to bring total pressure loss's change, which would influence each wheel's performance. When the counter rotating impeller's speed increases to 10,000RPM, the incidence angle increases further which results in a large production of swirl (which was inspected by pathlines of the channel). This swirl and the created heat generation lowers peak efficiency; when counter rotating speed decreases to 5,000RPM and 4,000RPM, swirl's effect on rotor impeller induced by counter rotor would be less serious. This may be an explanation of how the counter rotating wheel's speed affects the whole stage's isentropic efficiency.

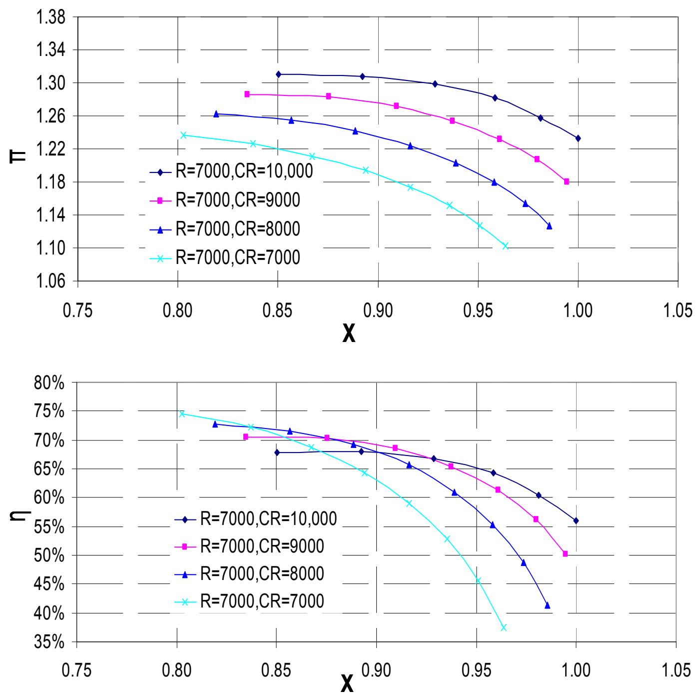

Figure 7 Total pressure ratio curve (upper) and isentropic efficiency curve (lower) at different r<1 rotational speed ratio (0.54ratio)

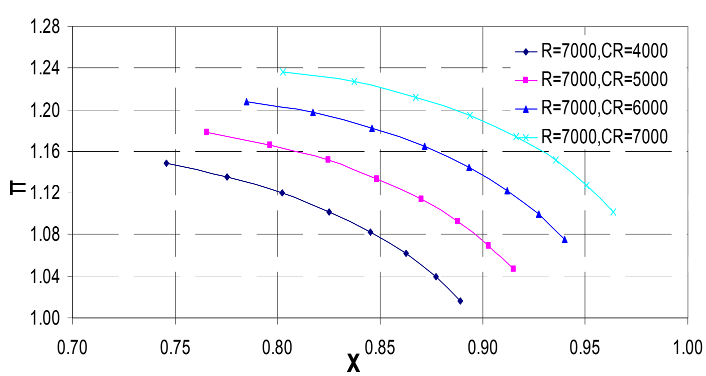

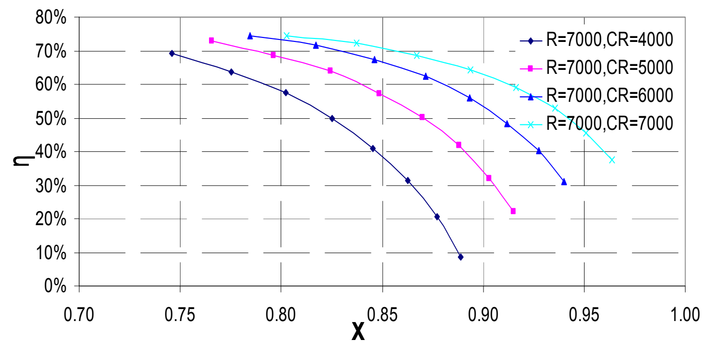

Figure 8 Total pressure ratio curve (upper) and isentropic efficiency curve (lower) at different r>1 rotational speed ratio (0.54ratio)

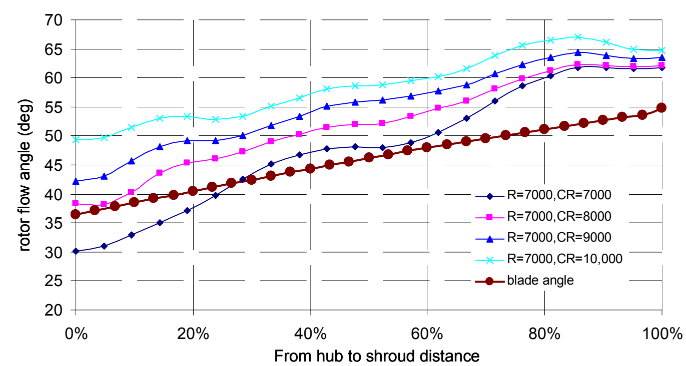

Figure 9 Flow angle and blade angle of the rotor at different rotating speed ratio stall point (0.54ratio)

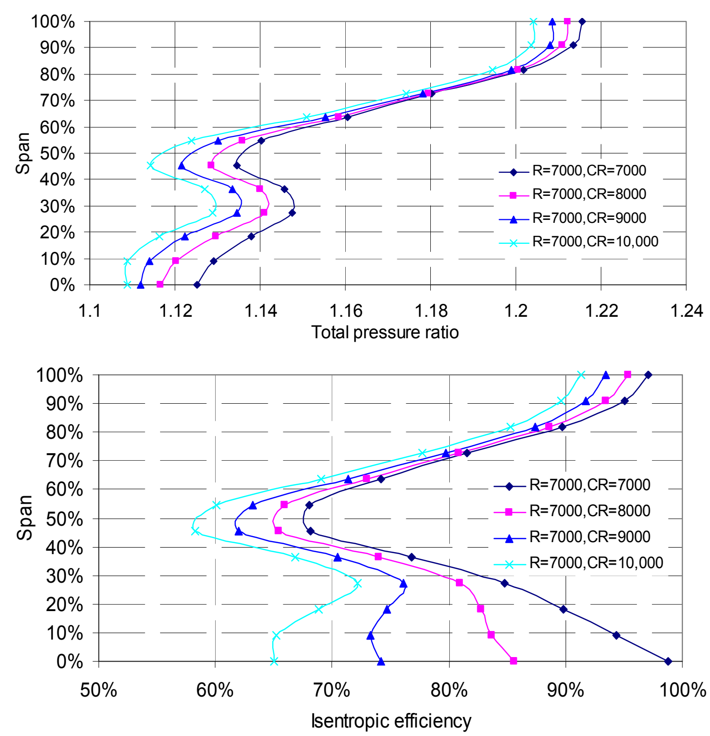

Figure 10 Rotor's pitch averaged total pressure ratio (upper) and isentropic efficiency (lower) at peak efficiency point (r<1)

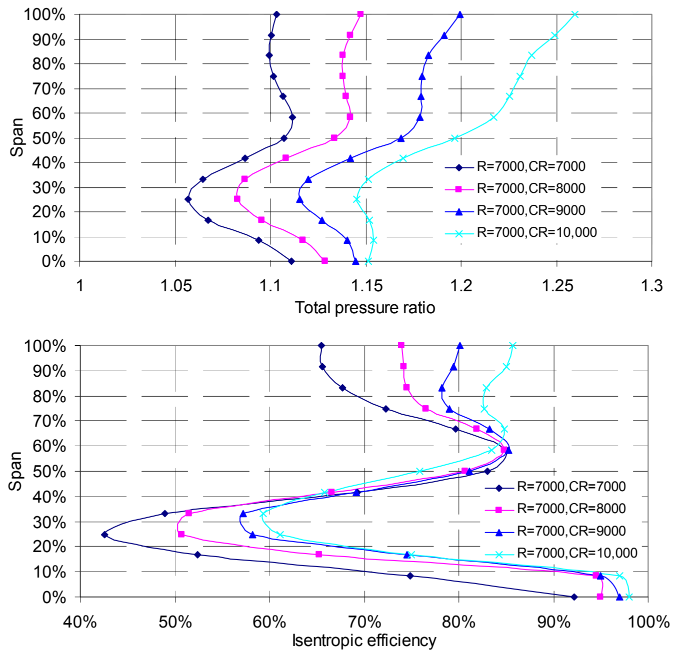

Figure 11 Counter rotor's pitch averaged total pressure ratio (upper) and isentropic efficiency (lower) at peak efficiency point (r<1)

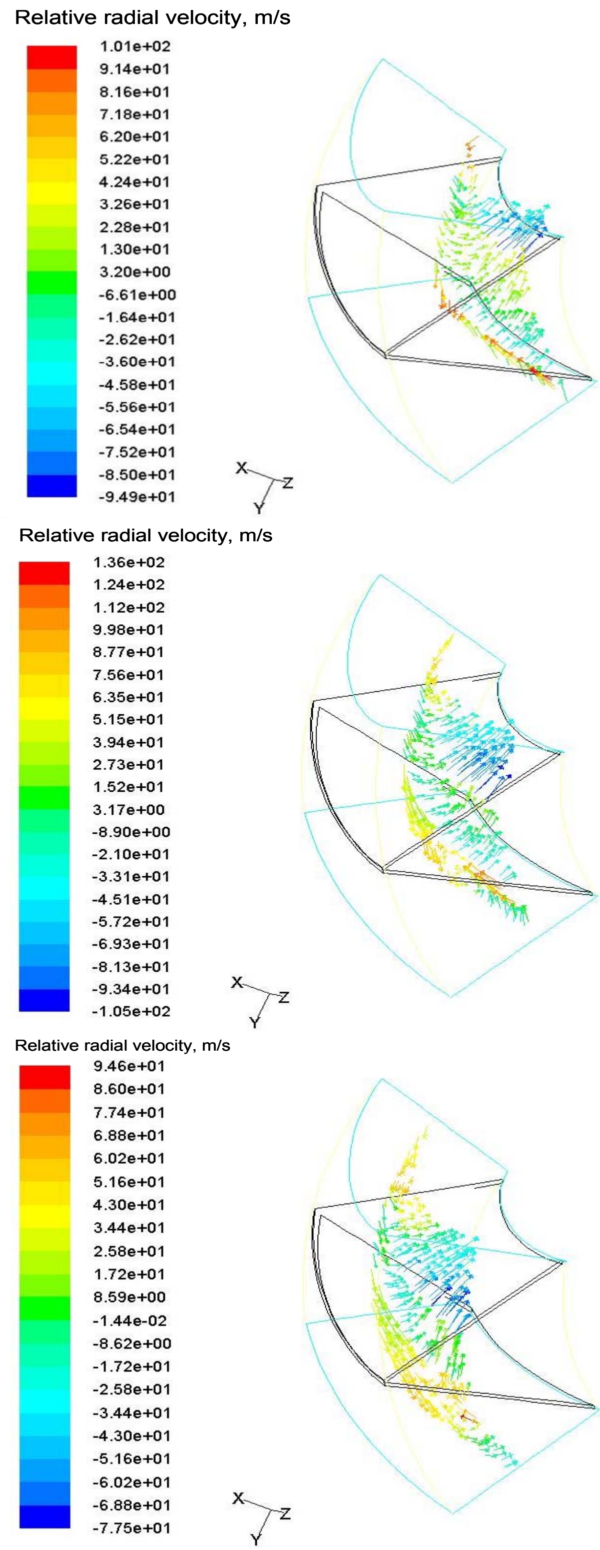

Figure 12 Comparison of rotor's radial velocity distribution at peak efficiency -- upper (30% span), center (45% span), lower (50% span)

To further analyze flow characteristics in the channel, circumferentially-averaged total pressure ratio and isentropic efficiencies for two rotating wheels are illustrated in Fig 10 and Fig.11. From Fig.4, it is shown that as blade angle increases, so does the tangential kinetic energy, which is later converted into pressure energy. Therefore, it is reasonable to have a continuously increasing pressure ratio and efficiency along the radial direction. However, distortions have been found in these performance curves and fluid separation can be attributed to this phenomenon. In the case of rotor channels at 30% span, as shown in Fig.12, the minimum relative radial velocity is about 95m/s, which opposes the main radial flow. This negative velocity basically forms a secondary flow and imposes a fluid separation from the impeller blade. This secondary flow generates heat and reduces pressure ratio's conversion from kinetic energy, as well as decreasing isentropic efficiency. In the case of the rotor channel at 45% span, this velocity increases further until it drops down dramatically at 50% span. Fluctuation of the amplitude reflects the change of incidence angle discussed previously, which also explains torsion curves in these figures to the left. It therefore can be concluded that this incidence angle's change plays an important role in producing a pressure loss brought on by secondary flow.

As mentioned previously, when counter-rotating speed increases, a large swirl will be induced in the rotor channels, which thus increases the incidence angle at rotor inlet, increasing heat generation and pressure losses. This explains the behavior seen in Fig.10, where the rotor's performance slightly decreases when the counter rotor's speed increases. This is counter-intuitive because a fast speed typically benefits the counter rotor's pressure ratio and efficiency.

In order to reduce the secondary flow's effect and improve impeller performance, it comes with a design of enlarging the hub/shroud ratio to 0.75 and maintaining the same blade angle, which is given in the following section.

Case 2 0.75 hub/shroud ratio

By increasing the H_d/S_d ratio to 0.75, steady-state performance curves are mapped in Fig.13 and 14. In these two figures, peak pressure ratios improve significantly, while the stable working range decreases. This is due to the contraction of the flow area. Since flow inside of the channel is subsonic; when flow crosses the critical cross section, the fluid accelerates and easily gets choked. In addition, the mass flow rate decreases at the surge point to reach the incidence angle when stall arises. This is the main reason why the performance map shifts to the left and the stable working range narrows. When the counter rotating wheel's speed is the highest, the same phenomenon, as in Case 1, can also be observed: stable working range is the narrowest. At the same time, the larger of H_d/S_d ratio, the larger the average turning angle of blade. Thus, the amount of momentum transferred from blade to fluid will be greater, as will be the overall stage pressure ratio.

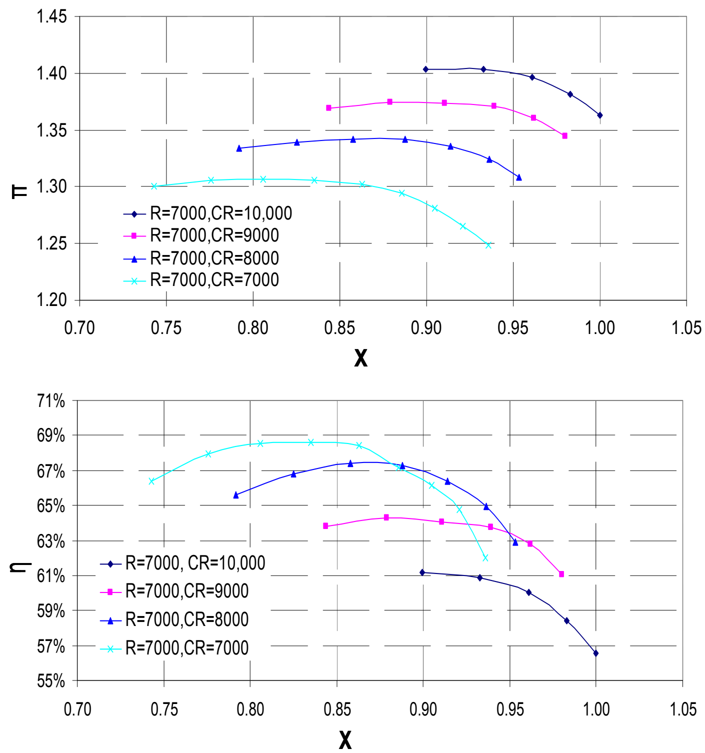

Figure 13 Total pressure ratio curve (upper) and isentropic efficiency curve (lower) at different r<1 rotational speed ratio (0.75ratio)

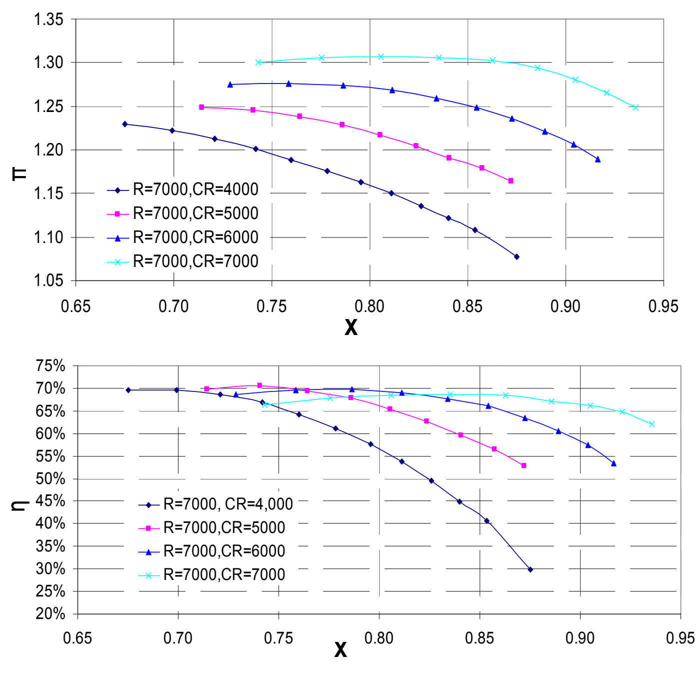

Figure 14 Total pressure ratio curve (upper) and isentropic efficiency curve (lower) at different r>1 rotational speed ratio (0.75ratio)

When compared with Fig.7, peak efficiency decreases from 75% in case 1 to 69% in case 2 where the speed ratio is less than 1. In addition, the efficiency map in case 2 has the trend that the lower speed relationship interestingly matches with the results at higher speed (Fig.13 right). The efficiency map is more sensitive to speed ratio, especially when it is less than 1. To further explain this phenomenon, detailed circumferentially averaged total pressure ratio and efficiency are plotted in Fig.15 and 16. Both pressure ratio and efficiency curves are still twisted but less than the smaller hub/shroud ratio case, especially for counter rotors. Comparing Fig.10 with Fig.11, it is interesting to note that distortion existed in Case 1 between span of 30% and 10%, which disappeared in Case 2: here only one distortion is found in Case 2, even though a large torsion exists at 50% span in both rotor cases. However, when two wheels rotate at the same speed of 7,000rpm, the efficiency difference from hub to shroud for case 1 is about 30%, whereas for case 2 it is only 20%. A large amount of the efficiency difference between the cases represents a large separation flow amount in the channel. By increasing the H_d/S_d ratio, performance has been improved throughout the rotor. In the counter rotor part of the stage, when comparing with variation of pressure ratio along with radial direction, Fig.16 (left) seems to be more serious than Fig.11 (left). This may be a result of a slight efficiency decrease in the whole stage. In addition, simply increasing hub/shroud tip ratio would change the design point which results the change of incidence angle and in order to improve isentropic efficiency, new blade angle optimization through CFD approach becomes necessary.

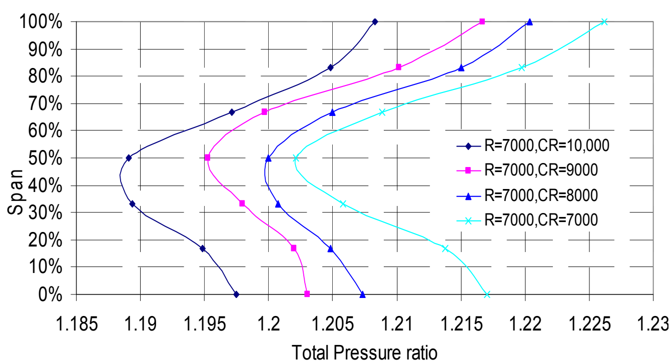

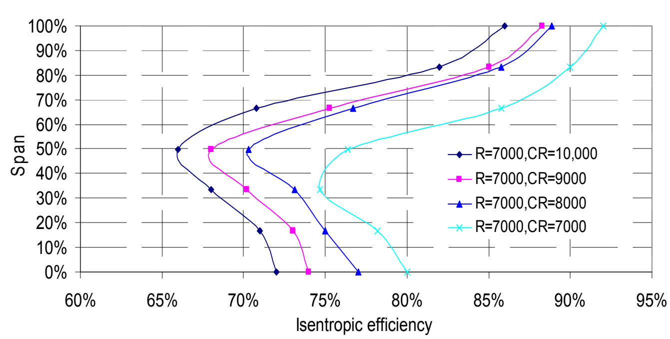

Figure 15 Rotor's pitch averaged total pressure ratio (upper) and isentropic efficiency (lower) at peak efficiency point (r<1)

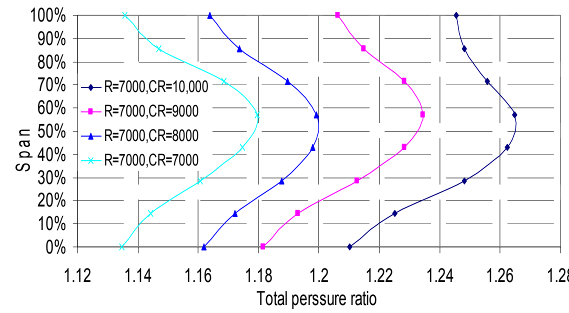

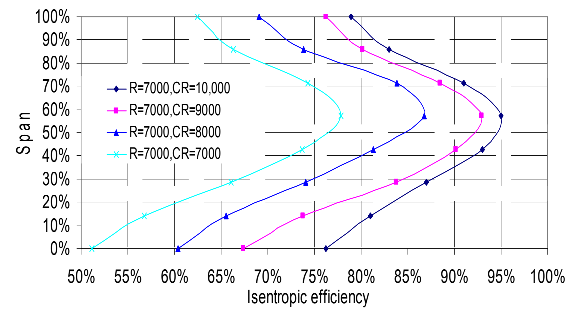

Figure 16 Counter rotor's pitch averaged total pressure ratio (upper) and isentropic efficiency (lower) at peak efficiency point (r<1)

Overall, it can be concluded that by increasing the hub/shroud diameter ratio, the stage pressure ratio increases significantly and magnitude of flow separation also got decreased, which resulted an overall improvement of each impeller's performance. Due to water vapor's temperature increasing and a further possible efficiency decreasing in following stages, idea of spraying evaporator's liquid water between compressor stages has been proposed by the group recently; sprayed liquid water is supposed to fully evaporate before entering of the second stage so that water vapor's temperature goes down and isentropic efficiency of entire compression process gets improved; as far as how this strategy is going to affect the whole multi-stage's performance, efforts are needed to continue this investigation.

Conclusion

A systematic analysis, in order to understand water vapor refrigerant's fluid flow characteristics in different hub/shroud diameter ratios of a novel axial counter rotating compressor, is carried out. To better demonstrate impeller's geometry, blade angle distribution is derived at the beginning. Specialties of the impeller pattern are given: with low manufacturing cost using a filament-winding, similar technology, the shroud has been integrated with the impeller. For this impeller, the blade angle is different from conventional ones, in that it is a curved line from hub to shroud and it is symmetric to its blade center rather than to impeller center. With 3D CFD, an optimized blade angle at a hub/shroud ratio of 0.58, performance curves are mapped. In order to further investigate flow characteristics, a single channel's performance is analyzed. Different speed ratios are also simulated for a better understanding of this novel axial impeller's performance. With the same blade angle distribution, the hub/shroud ratio increases to 0.75 to decrease the secondary flow's influence. Whole stage's performance curves as well as single channel's flow characteristics are also mapped. A comparison between these two hub/shroud ratios at different speed ratios is conducted to understand how to utilize this counter rotating technology to compress water vapor as refrigerant.

Using counter rotating technology, the stable working range narrows compared with general rotor-and-stator compressors, since stator vanes are not used directly after the rotor. At hub/shroud tip ratio of 0.58, stage pressure ratio has been found to be 1.24 with isentropic efficiency around 75% under subsonic flow conditions. Detailed flow structure inside of one channel shows that a significant secondary flow exists between 30% and 50% blade span. When hub-diameter/shroud-diameter ratio increases to 0.75, peak stage pressure ratio increases to 1.41 with a stage efficiency of 61%. The results also show the potential to apply counter rotating technology, using this novel impeller, to compress water vapor as refrigerant. However, further investigations are needed to improve the performance especially for a multi-stage inter-cooling configuration, e.g:

1) optimizing each stage's blade angle distribution
2) a mixture of different Hd/Sd shroud ratios for different stages is necessary from the consideration of wide stable working range, high pressure ratio and isentropic efficiency.

Nomenclature

H_d = hub's diameter
S_d = shroud's diameter
β_{inlet} = inlet blade angle relative to axial direction
β_{outlet} = outlet blade angle relative to axial direction
R = impeller radius
r = circular arc's radius
π = total pressure ratio
η_c = isentropic efficiency
χ = dimensionless of mass flow rate relative to specific point
p_{total} = total pressure
T_{total} = total temperature

REFERENCES

1. M.O. Mclinden, D.A.D., *Quest for alternatives.* ASHRAE Journal, 1987.
2. Demiss A. Amibe, Q.L., Norbert Mueller. *Multi stage variable speed turbo compressor for enhancing seasonal energy efficiency ratio of air conditioners using R718 as refrigerant*. in *ASME TurboExpo 2010*. 2010. Glasgow, UK.
3. Brandon F. Lachner Jr., G.F.N., Douglas T. Reindl, *The commercial feasibility of the use of water vapor as a refrigerant.* International Journal of Refrigeration, 2007. **30**(4): p. 699-708.
4. Eyler.A, N.M., *Simulation and production of wound impellers*, in *ASME-IMECE Paper 2008-51310*. 2008.
5. Li Qubo, J., Wang and N. Mueller, *On the realization of filament wound composite impeller for water refrigerant*, in *ASME Paper IMECE2009-12786*. 2009: Orlando.
6. Li Qubo, J.P., and Norbert Mueller, *Static, dynamic and failure behavior of a novel axial composite impeller for water chiller*, in *ASME-IMECE2010-39817*. 2010: Vancouver.
7. Li Qubo, J.P.a.N.M., *Aerodynamic design and CFD analysis of a novel axial compressor*, in *AIAA Fluid Dynamics* 2010: Chicago.
8. Li Qubo, R.G.a.M.N., *Using filament winding approach to manufacture composite impeller for water chiller.* Journal of advanced materials, 2010. **42**(4): p. 45-56.
9. Y.Y. Chen, B.L., Y Xuan and X.R.Xiang, *A study of speed ratio affecting the performance of a countra-rotating axial compressor.* Proceedings of the Institution of Mechanical Engineers, Part G: Journal of Aerospace Engineering, 2008. **222**(7): p. 985-991.
10. Young, R.H., *Countra-rotating axial fans.* J. Inst. Heat. Vent. Eng, 1951. **18**: p. 187.
11. Ernesto Benini, R.B., *Aerodynamic of swept and leaned transonic compressor-rotors.* Applied Energy, 2007. **84**: p. 1012-1027.
12. Nicolas Grourdain, S.B., Francis Leboeuf, Guy Jean Michon, *Simulation of rotating stall in a whole stage of an axial compressor.* Computers & Fluids, 2010.
13. N.Gourdain, S.B., F. Leboeuf, H.Miton, *Numerical simulation of rotating stall in a subsonic compressor.* Aerospace science and technology, 2006. **10**: p. 9-18.
14. Li Qubo, R.G., Mueller Norbert, *Using Filament Winding Approach to Manufacture Composite Impellers for Water Chiller.* Journal of Advanced Materials, 2010. **42**(4): p. 45-55.
15. Launder B, S.D., *The numerical computation of turbulence flow.* Comp Math Appl Mech Eng, 1974. **3**: p. 269-89.
16. Kui Jiao, H.S., Xianguo Li, Hao Wu, Eric Krivitzky, Tim Schram, Louis M. Larosiliere, *Numerical simulation of air flow through turbocharger compressors with dual volute design.* Applied Energy, 2009. **86**(11): p. 2494-2506.

12. Nicolas Grourdain, S.B., Francis Leboeuf, Guy Jean Michon, *Simulation of rotating stall in a whole stage of an axial compressor.* Computers & Fluids, 2010.

13. N.Gourdain, S.B., F. Leboeuf, H.Miton, *Numerical simulation of rotating stall in a subsonic compressor.* Aerospace science and technology, 2006. **10**: p. 9-18.

14. *ANSYS FLUENT 12.0 User's Guid*.

15. Launder B, S.D., *The numerical computation of turbulence flow.* Comp Math Appl Mech Eng, 1974. **3**: p. 269-89.